



Postseismic deformation following the April 25, 2015 Gorkha earthquake (Nepal): Afterslip versus viscous relaxation

François Jouanne, Ananta Gajurel, Jean-louis Mugnier, Laurent Bollinger, Lok Bijaya Adhikari, Bharat Koirala, Nathalie Cotte, Roshanraj Bhattarai, Pascale Bascou, Pascale Huyghe

► To cite this version:

François Jouanne, Ananta Gajurel, Jean-louis Mugnier, Laurent Bollinger, Lok Bijaya Adhikari, et al.. Postseismic deformation following the April 25, 2015 Gorkha earthquake (Nepal): Afterslip versus viscous relaxation. *Journal of Asian Earth Sciences*, 2019, 176, pp.105-119. 10.1016/j.jseaes.2019.02.009 . hal-03094658

HAL Id: hal-03094658

<https://hal.science/hal-03094658>

Submitted on 22 Oct 2021

HAL is a multi-disciplinary open access archive for the deposit and dissemination of scientific research documents, whether they are published or not. The documents may come from teaching and research institutions in France or abroad, or from public or private research centers.

L'archive ouverte pluridisciplinaire **HAL**, est destinée au dépôt et à la diffusion de documents scientifiques de niveau recherche, publiés ou non, émanant des établissements d'enseignement et de recherche français ou étrangers, des laboratoires publics ou privés.



Distributed under a Creative Commons Attribution - NonCommercial 4.0 International License

Postseismic deformation following the April 25, 2015 Gorkha earthquake (Nepal): afterslip versus viscous relaxation.

François Jouanne (1), Ananta Gajurel (2), Jean-Louis Mugnier (1), Laurent Bollinger (3), Lok Bijaya Adhikari (4), Bharat Koirala (4), Nathalie Cotte (1), Roshanraj Bhattarai (2,1), Arnaud Pecher (1), Pascale Bascou (1), Pascale Huyghe (1).

¹Univ. Grenoble Alpes, Univ. Savoie Mont Blanc, CNRS, IRD, IFSTTAR, ISTerre.

²Department of Geology, Tribhuvan University, Ghantaghar, Kathmandu, Nepal

³CEA, DAM, DIF, Arpajon, France.

⁴Department of Mines and Geology, National Seismological Center, Kathmandu, Nepal.

Abbreviated title suitable for page headings:

Postseismic deformation following the Gorkha earthquake.

Corresponding author:

François Jouanne,

Université de Savoie Mont Blanc, ISTerre,

F-73376 Le Bourget du Lac, France

Email : fjoua@univ-smb.fr

Tel : (33) 608371432

Abstract

The postseismic deformation consecutive to the April 25, 2015 Gorkha earthquake (M_w 7.9) is estimated in this paper based on a cGNSS network installed prior to the earthquake and supplemented by 6 cGNSS stations installed after the main shock. Postseismic displacements are obtained from daily time series corrected for interseismic deformation and seasonal variations. The maximum postseismic displacement is found north of the rupture area, where locally it reached 100 mm between the date of the earthquake and late 2016. The postseismic deformation affects the northern part of the rupture area but not the southern part, along the

southern part of the Main Himalayan Thrust (MHT). Three hypotheses for the mechanisms controlling postseismic deformation are tested through numerical simulations of the postseismic time series: (i) viscous relaxation, (ii) afterslip, or (iii) a combination of these two mechanisms. We can exclude postseismic deformation controlled by viscous relaxation of a thick deformation zone along the northern and lower flat of the MHT. However, it is impossible to discriminate between postseismic deformation controlled by either afterslip along the MHT (northern part of the rupture zone, crustal ramp, and lower flat of the MHT) or a combination of afterslip along the MHT (northern part of the rupture zone, crustal ramp) and viscous relaxation controlled by a thin (~3-4 km thick) low-viscosity body centered on the lower flat of the MHT. The occurrence of afterslip along the northern part of the upper flat of the MHT and its longitudinal variations have been established thanks to the densification of GNSS network by our team presented in this paper.

Introduction.

The large number of geophysical instruments which recorded the April 25, 2015 Mw 7.8 Gorkha earthquake provides a unique opportunity to document better than ever a large Himalayan earthquake. The main instrumental contributors to our understanding of the mainshock include Interferometric synthetic aperture radar (InSAR) investigations as well as teleseismic data (e.g. Avouac et al., 2015, Fan and Shearer, 2015), with also the continuous Global Navigation Satellite System (GNSS) time series (Grandin et al., 2015) and regional seismological records (e.g. Adhikari et al., 2015; Baillard et al., 2017). The deployment of the Nepal GPS Geodetic Network, prior to the earthquake, and its maintenance during the seismic crisis has also allowed to quantifying the early postseismic surface deformation (KKN4 and CHLM stations) consecutive to this large earthquake (Mencin et al., 2016; Gualandi et al., 2016).

In addition to being one of the few instrumental Himalayan earthquake, the setting of the 2015 earthquake (Fig. 1&2) is appropriate to study the complexity of the seismic cycle in a continental subduction zone. Indeed, the slip deficit along the main Himalayan thrust (MHT), on which the mainshock occurred, is accommodated during various types of earthquakes (Mugnier et al., 2013), that partially contributes to release the elastic strain accumulation (Avouac et al., 2015). This partial release has already been instrumentally measured in several oceanic subduction environments; for example, in the Andean convergent margin, the main slip patch of the 2010 Mw 8.8 earthquake occurred in an area that was highly coupled and had already released slip in 1960 (Melnick et al., 2012; Moreno et al., 2012). However, contrarily to earthquakes ruptures at oceanic subduction zones rarely captured by GNSS network in their whole extend due to their frequent extension offshore, the 2015 Gorkha rupture was surrounded by 12 stations well distributed above and around it. In addition, this permanent network was complemented during the weeks following the main shock, by the deployment of additional permanent or semi-permanent GNSS stations (this paper), this network dedicated to the postseismic deformation has been designed to test the occurrence of afterslip along the upper flat of the MHT in the rupture zone and south of it.

These records add some details to the postseismic deformation pattern and give a unique opportunity to study in greater details the mechanism controlling the postseismic deformation associated with the 2015 Gorkha event.

Different mechanisms are usually inferred for the postseismic deformation: afterslip or viscous relaxation. In this paper, the Relax software (Barbot et al., 2009) was used to model the postseismic deformation, taking into account the Main Himalayan Thrust geometry, rather well imaged in the region (Nabelek et al., 2009; Duputel et al., 2016) and the coseismic displacement field associated to it. Three postseismic mechanisms were tested: afterslip, viscous relaxation or a combination of these two phenomena. We used a flap-ramp-flat geometry (Elliott et al.,

2016) with a southern and upper flat corresponding to the geometry adopted by Grandin et al. (2015) to describe the coseismic slip distribution of the Gorkha earthquake along this flat.

Geological setting.

The structure of the Himalaya results from the underthrusting of the Indian lithosphere along the Main Himalayan Thrust (MHT) beneath the Tibetan Plateau (Argand, 1924). Great earthquakes have episodically ruptured segments of the brittle upper part of the MHT (e.g. Avouac et al., 2001; Mugnier et al., 2013, Bollinger et al., 2014). The Nepal earthquake of April 25, 2015 followed a series of great earthquakes in the Central Himalaya (Mugnier et al., 2011, Bollinger et al., 2016): over the last two centuries, the city of Kathmandu was severely damaged in 1833, 1866, and 1934.

The April 25, 2015 event (Fig. 1) was the first earthquake on the MHT to be simultaneously recorded by numerous instruments: high-rate GPS (e.g. Avouac et al., 2015), teleseismic waves (e.g. Fan and Shearer, 2015), SAR imaging (e.g. Lindsey et al., 2015), InSAR and teleseismic waves (Grandin et al., 2015), strong-motion recordings (e.g. Bhattarai et al., 2015), and a local seismometer network (Adhikari et al., 2015).

The rupture was mainly located to the NW of Kathmandu, at a depth of 13–15 km on a flat portion of the Main Himalayan Thrust (MHT) that dips N–NE at 7–10°. The northern boundary of the main rupture corresponds to the transition towards a steeper crustal ramp. This ramp, which is partly coupled during the interseismic period (Jouanne et al., 2017), was only locally affected by the earthquake (Elliott et al., 2016). The southern boundary of the rupture was near the leading edge of the Lesser Himalaya antiformal duplex (Mugnier et al., 2017) and possibly near the frontal footwall ramp of the upper Nawakot duplex (Hubbard et al., 2016). This rupture was affected by transversal structures: on the western side, a ~20° dipping lateral ramp (Kumar et al., 2017), located beneath the Judi lineament (Mugnier et al., 2017) and already defined by

Kayal (2008), separates the main rupture zone from the nucleation area. On the eastern side, a lateral ramp (Mugnier et al., 2017) located beneath the Gaurishankar lineament (Kayal, 2008) illustrated by its seismic signature at depth (Letort et al., 2016, Baillard et al., 2017) separates the April 25, 2015 rupture from the May 12, 2015 (Mw 7.2) rupture.

Data acquisition and analysis.

After the April 25 Gorkha earthquake, we installed a GNSS network designed to record postseismic deformation induced by this Mw 7.9 earthquake. We installed four permanent GNSS stations in June 2015 and 11 campaign GNSS stations between June and December 2015. Seven of these stations were measured again in November 2016 (Figs 3 and 4). We analyzed these data together with the continuous GNSS networks established by LDG-DASE, Caltech (www.unavco.org), Central Washington University (<http://www.geodesy.cwu.edu>) and with data from the GNSS sites defined in the ITRF2014 reference frame (Altamimi et al., 2016) (ARTU, BADG,BAKU,BJFS, BJNM, CHUM, CUSV, GUAO, HYDE, IISC, IRKJ, IRKM, KIT3, KUWT, LHAZ, MDVJ, POL2, SGOC, SHAO, TALA, TASH, TCMS, TEHN, TNML, URUM, ZECK) obtained from unavco.

The data were analyzed using Bernese 5.2 software (Dach et al., 2016) with absolute antenna phase center offset models, together with precise IGS orbits, Earth rotation parameters, and ocean tidal loading and atmospheric tidal loading estimates. Velocities and time series were estimated in the ITRF2014 reference frame (Altamimi et al., 2016) with discontinuities associated with this reference frame and expressed in terms of the India fixed reference frame by the use of the rotation pole proposed by Ader et al. (2012). This rotation pole, originally proposed to describe the motion of India relative to ITRF2005, accurately describes the India plate motion in the ITRF2014 reference frame, as shown by Jouanne et al. (2017) and as

exemplified by the lack of velocity of the cGPS SIM4 station located on the India plate (Fig. 3). In any case, any velocity changes introduced by the ITRF2005 / ITRF2014 change are negligible compared to the large postseismic displacements.

We followed the resolution strategy with (1) an initial ionosphere-free analysis with calculation of the residuals; (2) a residual analysis; (3) code-based wide-lane ambiguity resolution for all baselines (Melbourne, 1985; Wübbena, 1985), using differential code bias (DCB) files when available and calculation of the ionosphere-free solution with the introduction of resolved Melbourne-Wübbena linear combination ambiguities; (4) phase-based wide-lane (L5) ambiguity resolution for baselines < 200 km and computation of the ionosphere-free solution with the introduction of resolved ambiguities; (5) resolution of the previously unresolved ambiguities for baselines < 2000 km using the quasi ionosphere-free strategy of resolution; (6) direct L1/L2 ambiguity resolution for baselines < 20 km with the introduction of an ionosphere model; (7) calculation of the normal equations; (8) a compatibility test between the daily free solution and ITRF2014 solution, selection of compatible ITRF2014 stations, and (9) transformation of the daily normal equation in the ITRF2014 reference frame with a six-parameter Helmert solution (three translation parameters and three rotation parameters) using the ITRF2014 selected stations. During these steps, site-specific troposphere parameters were estimated every two hours.

Normal equations were analyzed simultaneously to determine accurate velocities in the ITRF2014 reference frame with the introduction of ITRF2014 coordinates and velocities. Outliers and new discontinuities were detected using the “Find Outliers and Discontinuities in Time Series” tool in Bernese 5.2 software which estimates annual seasonal fluctuations and reduces, step by step, the discrepancy between the functional model and the time series due to statistical adjustment (Ostini et al., 2008). Bernese 5.2 software underestimates the daily errors because systematic errors or mismodeled parameters are not included in the formal error. We

therefore rescaled the formal errors by multiplying them by a factor of 10 to obtain a more realistic estimated error (Hugentobler et al., 2001).

Results: postseismic displacements at the surface.

We consider that displacements contain three superimposed signals: interseismic displacements, postseismic displacements, and the seasonal signal associated with loading of the Ganga Plain during the monsoon and its unloading during the dry season (Bettinelli et al., 2008; Fu and Freymueller, 2012; Gualandi et al., 2016). In order to analyze postseismic displacements, we removed the interseismic displacements that were either measured before the Gorkha earthquake for the sites that already existed before this event (BESI, BRN2, CHLM, DAMA, GUMB, KKN4, KLDN, LMJG, NAST, ODRE, RMJT, RMTE, SNDL, SYBC, TPLJ) (Fig. 2; Jouanne et al., 2017) or were estimated using interseismic deformation modeling by Jouanne et al. (2017) for the new GNSS sites (Fig. 3).

In order to evaluate the seasonal components, we make the hypothesis that time series are nearly linear during the period beginning 300 days after the 25 April 2015 earthquake. For the period beginning 300 days after the main shock, we have then modeled time series as the consequence of a linear velocity and of seasonal component (eq. 1).

$$U(t) = U^*(t-t_{\text{ref}}) + a \cos(2\pi^*(t-t_{\text{ref}})/365) + b \sin(2\pi^*(t-t_{\text{ref}})/365) + c \cos(2\pi^*(t-t_{\text{ref}})/182.5) + d \sin(2\pi^*(t-t_{\text{ref}})/182.5) \quad (\text{eq. 1})$$

Where t_{ref} is the first date after the day D_0+300 existing in the time series, D_0 being the date of the main shock, U the velocity, and a , b , c and d are the amplitude of annual and semi-annual signals. In a second step, whole time series are corrected for seasonal signals using these amplitudes.

The postseismic displacements for the period when most of the GNSS stations were available (between June 24, 2015 and late 2016) are shown (Fig. 4) to compare site displacement measured over the same time span. Postseismic displacements are characterized by the southward displacements of the points north of the Gorkha rupture (CHLM, GUMB, TSM1). The station that recorded the greatest postseismic displacement is CHLM (Fig. 4 and 5) located to the north of the rupture, with 40 mm of southward displacement between April 25 and June 24, 2015 and 100 mm of southward displacement between June 24, 2015 and late 2016. The points located in the northern part of the rupture zone (KKN4, GURJ, BALE) are affected by moderate southward postseismic displacements, whereas the points located at the southern end of the rupture, near to and south of Kathmandu (CHIR, DAMA, NAST and XYAK), are subject to small postseismic displacement. It should be noted that the points at the western part of the rupture (LMJG, GORK and ANBU) are not affected by postseismic displacements whereas the points located several kilometers to the east of the April 25, 2015 rupture (CHAR, JIR2, MALU) are affected by significant postseismic displacements reaching 35 mm (Fig. 4). Given that these points were installed after the Mw 7.2 main aftershock of May 12, 2015, these postseismic displacements could be related to the postseismic deformation induced by this earthquake, but the lack of change in the cumulative postseismic displacements in the CHLM time series indicates, before and after the May 12, 2015 earthquake indicates that this second large earthquake does not induce a significant postseismic deformation. Significant postseismic displacements are therefore restricted to the northern part of the rupture zone and to an area to the north of it (Figs 4, 5, 6 and 7). It is important to note that there are no clear postseismic displacements to the south of the Gorkha earthquake rupture and, like Mencin et al. (2016), we exclude the occurrence of significant afterslip along the southern part of the MHT. Therefore, the slip deficit along the MHT south of Kathmandu is not resorbed aseismically by slip along the MHT from the rupture zone to the MFT where the MHT emerges.

The slip deficit could then possibly be resorbed by a future large earthquake between the southern end of the rupture near Kathmandu and the Main Frontal Thrust near the Ganga Plain, as probably happened in the 1866 earthquake (Oldham, 1883; Szeliga et al., 2010), or by a larger earthquake rupturing the locked fault zone from the brittle-ductile transition zone to the surface, in a similar way as in the subduction zones (Melnick et al., 2012; Moreno et al., 2012) or to the 1934 Nepal-Bihar earthquake (e.g. Mugnier et al., 2013).

Figures 5, 6 and 7 illustrate the postseismic deformation with the time series for the southern, eastern and vertical components corrected for the interseismic component and the seasonal signal in the India fixed reference frame.

Time series of southern component present a progressive decrease in postseismic displacement with time, suggesting progressive dissipation of the stress perturbation induced by the earthquake (Fig. 5). It can be observed that the time series of the eastern components (Fig. 6) presents spatial variations: BALE, CHLM and DNC4 time series indicate significant westward components of postseismic displacements, whereas time series of BHAZ, CHAR, GUMB, JIR2, KKN4 and XBAR do not present this component. This is why we will consider only the southern and vertical time series to simulate postseismic displacements. Time series of vertical component present a progressive decrease in postseismic displacement with time, suggesting progressive dissipation of the stress perturbation induced by the earthquake (Fig. 7). The CHLM time series of the south components presents a jump corresponding to the Mw 7.2 main aftershocks of May 12, whereas the other stations were not significantly affected or were installed too late to record this coseismic displacement. It can be also observed that this second earthquake does not induced a change in the evolution of the postseismic displacement of the CHLM and KKN4 station. This is why we have not consider this earthquake in the numerical simulations.

Modeling postseismic- displacement.

We have chosen to test the origin of the progressive release using three hypotheses with Relax 1.0.7 software (Barbot et al., 2008; Barbot et al., 2009; Barbot and Fialko 2010; Bruhat et al., 2011; Rousset et al., 2012): a postseismic deformation controlled by afterslip, viscous relaxation of the stress perturbation with a linear rheology, and a combination of these two mechanisms.

This software computes the displacement and stress due to dislocations and the nonlinear postseismic time-dependent deformation, the latter either controlled by viscous bodies or by rate-strengthening friction faults. This software takes gravity into account and is based on a Fourier-domain elastic Green's function and an equivalent body-force representation of deformation mechanisms. We consider a 512*512*512 grid size model around the relevant faults with 0.7*0.7*0.7 km sampling which corresponds at a 358*358*358 km grid.

For this modeling, we use the same MHT geometry as for the pre-earthquake deformation (Jouanne et al., 2017); this geometry also fits with the location of the rupture zone proposed by Grandin et al. (2015) indicated in Figure 2. The geometry of the MHT is formed by a succession of flats and ramps characterized by a large southern flat (95–100 km) dipping 7° northward, a crustal ramp dipping 27° northward between 15 and 25 km, and a northern flat dipping 7° northward as illustrated by receiver-function data (Duputel et al., 2016).

As postseismic displacements only affected stations north of Kathmandu, if postseismic displacements are controlled by afterslip along the MHT, afterslip did not affect all of the upper flat of the MHT but only its northern parts. If we consider the points BALE, KKN4, and GURJ (Fig. 4 and 5) that are nearly the same distance from the upper flat-ramp connection, it appears that the eastern one (BALE) is affected by greater postseismic displacements than the other two located in the western part of the upper flat of the MHT. We then considered that these surficial variations in displacement reflect afterslip distribution along the MHT. These spatial variations

in the time series led us to consider a 25 km-wide western segment and a 40 km-wide eastern segment and the boundary between these two segments coincides with the western edge of the May 12, 2015 rupture and with the Gaurishankar lateral ramp as illustrated in Figure 1. This spatial variation also reflects interseismic coupling variations between the western and eastern parts: the western part was completely locked whereas the eastern part was only partially locked, with a coupling of 0.7 (Fig. 2a) (Jouanne et al., 2017).

To test the models, we used a time series that was corrected for interseismic velocities and seasonal components. As postseismic displacements are southward with a lack of E-W components, we have only used the N-S and vertical components of time series.

The preferred solutions were selected using the comparison between the observed and simulated time series with the estimation of weighted root mean square WRMS for each simulation (Fig. 9).

Viscous relaxation model.

The estimation of coupling during the interseismic period (Betinelli et al., 2006; Ader et al., 2012; Jouanne et al., 2017) suggests ductile behavior along the northern flat of the MHT. We therefore test the hypothesis that postseismic displacements reveal viscous relaxation of the stress perturbation induced by the main shock. Ductile behavior is temperature dependent (Scholz, 1998) and does not occur in the brittle crust. Viscous relaxation is therefore excluded for the upper flat and the ramp characterized by a temperature of less than 375 °C (Robert et al., 2011). Hereafter, we assume that the lower flat accommodates viscous relaxation only.

In this simulation, a low viscous body with a linear Maxwell rheology corresponding to the deeper part of the Main Himalayan Thrust is embedded in an elastic half space (Fig. 8a). The parameters to be determined are the viscosity and the thickness of this body. As the indian

lithosphere is very thick, 135 km in eastern Nepal (Devi et al., 2011), we do not take into account the asthenosphere viscosity.

We chose to explore the following ranges of values: viscosity of the body from 10^{16} to 10^{19} Pa*s and thickness of the body from 0 to 14 km. The WRMS is invariably greater than 17 mm and no solution is clearly favored among the 84 numerical runs performed to determine parameter influence and summarized in Figure 9a.

Afterslip model.

If the postseismic displacements are controlled by afterslip induced by the Mw 7.9 earthquake of April 25 2015, these displacements can be simulated by progressive release of stress perturbation due to the main shock. We assume that the afterslip occurs (Fig. 8a) along the northern part of the upper flat of the MHT affected by the April 25, 2015 earthquake, along the crustal ramp north of the rupture zone, and along the lower flat north of this ramp.

We assign rate-strengthening properties derived from laboratory experiments (Dieterich, 1979; Ruina, 1983, Barbot et al., 2009; Lapusta et al., 2000; Rice & Ben-Zion, 1996) to these three fault segments with:

$$V = 2 \dot{\gamma}_0 \sinh \frac{\Delta\tau}{(a - b)\sigma} \quad (\text{eq. 2})$$

Where V is the slip velocity on the fault, $\Delta\tau$ is the shear stress perturbation induced by the earthquake that is progressively released by the afterslip, $\dot{\gamma}_0$ is the initial slip velocity and $(a - b)$ σ is a constitutive parameters with a value of the order of the stress drop during the earthquake, σ being the effective normal stress and $(a - b)$ a frictional parameter.

The initial stress perturbation associated with the coseismic slip distributions of April 25, 2015 estimated by Grandin et al. (2015), with InSAR and teleseismic waves data (Fig. 2b) is calculated with Relax 1.0.7 software.

305 We explore the parameters space (Fig. 9b, c, d) formed by $\dot{\gamma}_0$ (from 50 to 500 mm/year), and
306 the friction along the relevant planes (from 0.2 to 0.7) for $(a - b)$ σ values of 10 and 22 MPa (22
307 MPa being the stress drop estimated by Denolle et al., 2015). The tests of the $(a - b)$ σ values
308 of 22 and 10 MPa (Fig. 9 c and d) allow us to determine that the best fit for the southern
309 component time series is obtained for the $(a - b)$ σ value of 22 MPa, which is the value of the
310 stress drop estimated by Denolle et al. (2015), a friction ratio of 0.7 and a $\dot{\gamma}_0 = 200$
311 mm/year. The simulation of vertical time series allows to confirm that $\dot{\gamma}_0$ must be larger than
312 150 mm/year (Fig. 9d).
313 We decide to adopt as the better model the solution obtained for 0.7 frictional parameters and
314 a $\dot{\gamma}_0$ value of 200 mm/year.

315

316 *Afterslip and viscous relaxation model.*

317 This simulation takes into account the hypothesis that the northern flat may be a zone affected
318 by ductile deformation (Beaumont et al., 2001), while the upper part of the MHT is probably in
319 a brittle condition as shown by the high coupling of the upper flat and crustal ramp during the
320 interseismic period (Jouanne et al., 2004; Ader et al., 2012; Jouanne et al., 2017).

321 We test the hypothesis of a mixed origin for postseismic deformation (Fig. 8), with viscous
322 relaxation controlled by a deep low-viscosity body centered on the northern MHT flat, as done
323 above, whereas afterslip occurs along the crustal ramp and the northern part of the southern flat.
324 We adopt, as an *a priori* model for the afterslip component, the above model that minimizes
325 the WRMS among the models based solely on afterslip and we explore the following
326 parameters: viscosity of the low-viscosity body (from 10^{16} to 10^{19} Pa.s) and the thickness of
327 this body (1 to 6 km).

328 Among 50 numerical runs performed to determine the parameter influence with the southern
329 time series (Figure 9e), a minimum of 3.2 mm is found for the WRMS (Fig. 9e) linked to a 3-4

km thickness for the viscous body and a 10^{16} Pa*s viscosity. The used of vertical component to determine the best solution (Fig. 9 e) is not determining.

Discussion.

Comparison between the different models.

Comparison of the WRMS for the models performed with the three hypotheses tested (Fig. 9) indicates that the models with only viscous relaxation on the lower flat of the MHT have much higher WRMS and can be excluded (Fig. 9a).

The other two models, afterslip alone or afterslip associated with viscous relaxation on the lower flat of the MHT, have respectively WRMS for the southern time series of 3.6 mm for the afterslip model and of 3.2 mm for the mixed model. The use of vertical time series (Fig. 9d and 9f) do not help to choose between these two models.

The mixed model seems to better simulate the observations than the afterslip only model, but if the Relax software allowed the use of variable friction coefficients along the MHT, it would probably be possible to find a more satisfactory solution with the afterslip model, with probably a lower friction coefficient along the northern flat of the MHT than along the ramp and the southern or upper flat of the MHT.

Therefore the numerical modeling approach does not enable us to choose between the two hypotheses – afterslip alone or afterslip combined with viscous relaxation on the lower flat (Fig. 9c and 9e and Fig. 10). Nevertheless, it must be underlined that afterslip combined with viscous relaxation on the lower flat allows to simulate the early postseismic displacements as shown on Figure 10 for the CHLM and KKN4 time series which is not the case if we consider the afterslip only model.

All the retained simulations indicate (Fig. 9c and d, Fig. 9 e and f, Fig. 11 and 12): (a) moderate afterslip along the ramp; (b) significant afterslip along the northern part of the upper flat; (c)

substantial afterslip where the coseismic slip gradient was high: at the upper flat/crustal ramp transition, locally in the rupture area, and near the southern boundary of the rupture. Afterslip along the southern part of the upper flat, to the south of the southern border of the numerical model, has been a priori excluded in our modelling as it has suggested by the near zero postseismic displacement measured in the southern part of the Gorkha earthquake rupture zone. This observation indicates the likely existence of local variations in friction coefficients not taken into account in our model.

Afterslip properties along the MHT.

With Relax software it is possible to consider just one single afterslip property (friction ratio and constitutive parameters) for all of the fault segments. As a result, we then considered the same properties for the upper flat, crustal ramp, and lower flat of the MHT. Our preferred model, which provides a good fit with the observed time series (Fig. 7c), was obtained with $\dot{\gamma}_0 = 200$ mm/year and a friction of 0.7 for (a-b) $\sigma = 22$ Mpa.

A friction coefficient of 0.7 is somewhat higher than the values usually inferred. For example, the friction angle was estimated at 20° for the Indian crust in modeling by Berger et al. (2003). Such high values have nonetheless been found experimentally for numerous rocks (Kulhawi, 1975).

The afterslip evolution over time and space of our preferred model indicates that (Fig. 11): the lower flat of the MHT is affected by slow large-scale afterslip decreasing over time, whereas the crustal ramp is affected by negligible afterslip without significant lateral variations. The northern part of the upper flat is characterized by local patches of high afterslip; the latter reached 1 m after two years with significant lateral variability and a significant decrease of afterslip evolution between $D + 30$ days and $D + 6$ months. The areas of the upper flat affected by significant slip are located close to the flat-ramp transition corresponding to the northern

boundary of the rupture. Areas of the upper flat locally affected by significant slip are characterized by a local high coseismic displacement gradient in Grandin et al.'s model (2016) and then by local high deviatoric stress to be released. Locally, slip also occurred southward, in areas near the southern end of the mesh, the upper flat segment of the MHT affected by afterslip. Our modeling suggests changes of width of the upper flat of the MHT affected by afterslip (Fig. 11). The distribution of the afterslip reflects the distribution of the coseismic displacement model, the roughness of the afterslip distribution reflects the roughness of the co-seismic displacement model considered at the input of the model. It can therefore be assumed that with a smoother coseismic displacement model, we would also obtain a smoother afterslip model. But we assume that the model roughness considered as input does not affect the conclusions of our models.

Our modelling clearly differs from the model proposed by Wang and Fialko, 2018, we allow afterslip along the northern part of the 2015 rupture whereas these authors supposed that no afterslip occurred along the upper flat of the MHT. Our model allows good simulation of time series of points located in the southern part of the area affected by postseismic deformation BALE, BHAZ, GURJ, KKN4, JIR2 and CHAR whereas the model of Wang and Fialko does not allow a good simulation of the time series of JIR2, the points BALE, BHAZ, GURJ and CHAR, installed by our team, being not included in their study. On the contrary, the model of Wang and Fialko presents a better simulation of the CHLM and DCN4 time series. Our model failed to predict accurately the early postseismic deformation of CHLM and failed to well fit the time series of DCN4 and GUMB. We can then propose that rheological properties are different between the upper flat of the MHT and the crustal ramp and the northern flat. As in this study we present a larger number of time series sensitive to the afterslip along the upper flat, we can suppose that our solution reflects mainly the rheological properties of the upper flat

whereas the results presented by Wang and Fialko, 2018 reflect mainly the rheological properties along the lower part of the MHT (ramp and northern flat).

Viscous relaxation controlled by a low viscosity zone along the lower flat of the MHT.

The time series for the stations located above the rupture zone, or to the south of it, are not correctly simulated by only viscous relaxation controlled by a ductile body centered on the northern flat. In the numerical models where afterslip along the upper flat of the MHT and along the crustal ramp has been introduced, the low-viscosity body (10^{16} Pa.s) has to be thin (close to 3-4 km) to minimize the discord between model and data (Fig. 9e). We therefore believe that viscous relaxation controlled by a low-viscosity body cannot alone explain the recorded postseismic deformation and another source of deformation located to the south of the lower flat (i.e. afterslip) is needed. Models combining afterslip and viscous relaxation controlled by a thin, viscous body centered on the lower flat of the MHT better predict early post-seismic displacement (CHLM and KKN4 time series) than models considering only afterslip along the MHT (Fig. 10).

The low-viscosity body is a reasonable assumption as it may explain the low coupling along the lower flat documented for the interseismic period (Fig. 2a and 12). Furthermore, the low-viscosity level has been suggested from the interpretation of deep images of the Himalayan crust (e.g. Zhao et al., 1993; Nelson et al., 1996). Since these articles, new seismic experiments demonstrated that the low velocity zones in Tibet is discontinuous, restricted to surfaces with maximum vertical extension of 10 km and maximum horizontal length about 50 km (Hetenyi et al., 2011).

A channel flow model (Beaumont et al., 2001) was even proposed to describe the evolution of Himalayan tectonics and is based on a very thick ductile zone (more than 10 km thick); so thick

that the horizontal velocity depicts a peculiar gradient, with a maximum velocity in the center of the ductile zone. Our results nonetheless suggest that the ductile zone is 3 – 4 km thick beneath the extreme southern part of the Tibetan plateau. Therefore, we suggest that the recent tectonism of the Himalaya is not controlled by channel flow deformation at depth, although our results does not preclude a thicker ductile zone to the north.

If we assume that postseismic deformation ends after 6 years, our results (Fig. 12) show (1) afterslip or viscous relaxation of a thin body (~3-4 km thick) of low viscosity along the lower flat of the MHT (up to 0.5 m after 6 years) and (2) moderate afterslip along the crustal ramp that extends down-dip from the Gorkha rupture (up to 0.5 m after 6 years) as well as (3) a high-velocity small-scale afterslip (up to 5 m after 6 years for the western segment) along the southern boundary of the upper flat affected by afterslip, and along the upper flat, high-velocity afterslip in areas characterized by a significant coseismic slip gradient during the earthquake (reaching 5.6 m after 6 years in its western part and 3.4 m in its eastern part).

This pattern, in which moderate afterslip occurs along the crustal ramp and extends down-dip from the rupture, has also been shown for the postseismic deformation following the 2005 Balakot-Bagh earthquake (Jouanne et al., 2011; Wang and Fialko, 2014), for the deformation consecutive to the 1995 Chi-Chi earthquake (Yu et al., 2003; Perfettini and Avouac, 2004), and for the 1995 Jalisco earthquake (Hutton et al., 2001).

Importance of afterslip in the seismic cycle.

As illustrated in Figure 12, the effects of afterslip consecutive to the Gorkha earthquake remain confined to the northern part of the rupture area, the crustal ramp, and the northern flat of the MHT. The afterslip does not, then, homogenize coseismic slips throughout the rupture area but

only and partially in its northern part. Moreover, if we consider that the 1833 and 2015 earthquakes have the same rupture area, and if we take the cumulated slip along the MHT during the interseismic period as estimated by Jouanne et al. (2017), then it appears that postseismic displacement along the MHT does not homogenize slip along the MHT between the ductile slip along the northern flat (4 m for 200 years) and the coseismic slip along the northern part of the upper flat.

Conclusion.

The cumulative postseismic velocity field clearly shows a lack of displacements to the south of Kathmandu. Afterslip along the southern part of the rupture area of the Gorkha earthquake and along the southern segment of the MHT, that was unaffected by the main shock, is then clearly excluded. The slip deficit along the southern part of the upper flat of the MHT, between Kathmandu and the Ganga Plain, would probably be transferred along the MHT by an earthquake of large magnitude, as may have been the case after the previous 1833 large earthquake along this segment of the MHT, or by a very large magnitude earthquake affecting the MHT from the ductile zone to the MFT. To the west and east of the Gorkha rupture, postseismic displacements are almost negligible, and afterslip does not affect the upper flat areas of the MHT to the west of the rupture zone.

The simulation of the time series using Relax software suggests that the postseismic deformation consecutive to the April 25, 2015 earthquake is controlled by: heterogeneous afterslip along the northern part of the upper flat of the MHT corresponding to the northern part of the rupture; afterslip along the crustal ramp reaching 0.17m after two years; and afterslip reaching 0.20 m after two years or viscous relaxation of a thin (~3-4 km thick) ductile zone along the lower flat of the MHT. Viscous relaxation along a ductile body centered on the lower flat of the MHT alone cannot explain alone the postseismic deformation.

479

480 Acknowledgments.

481 The figures and maps were prepared using Generic Mapping Tools software (Wessel
482 and Smith, 1995) and Paraview software (Ahrens et al., 2005; Ayachit, 2015). This material is
483 partially based on data provided by the Nepal permanent GNSS network (DMG, Caltech,
484 DASE) and data services provided by the UNAVCO Facility with support from the National
485 Science Foundation (NSF) and National Aeronautics and Space Administration (NASA) under
486 NSF Cooperative Agreement No. EAR-0735156. Funding was from the Labex OSUG@2020,
487 INSU-CNRS, the AAP of Savoie Mont Blanc University, the IRD, and the ANR Bhoutanepal.
488 We thank two anonymous reviewers for their detailed and constructive reviews.

489

490 References

491 Ader, T., Avouac, J.P., Liu-Zeng, J., Lyon-Caen, H., Bollinger, L., Galetzka, J., Genrich, J.,
492 Thomas, M., Chanard, K., Sapkota, S., Rajaure, S., Shrestha, P., Ding, L., Flouzat, M., 2012.
493 Convergence rate across the Nepal Himalaya and interseismic coupling on the Main Himalayan
494 Thrust: implications. *J. Geophys. Res.* 117, B04403. <http://dx.doi.org/10.1029/2011JB009071>.
495
496 Adhikari, L.B., Gautam, U.P., Bhattarai, M., Kandel, T., Gupta, R.M., Timsina, C., Maharjan,
497 N., Maharjan K., Dahal, T., Hoste-Colomer, R., Cano, Y., Dandine, M., Guilhem, A., Merrer,
498 S., Roudil, P., Bollinger, L., 2015. The aftershock sequence of the April 25 2015 Gorkha-Nepal
499 earthquake. *Geophys. J. Int.* 203, 2119–2124.
500
501 Ahrens, J., Geveci, B., Law, C., 2005. *ParaView: An End-User Tool for Large Data*
502 *Visualization*, Visualization Handbook, Elsevier, ISBN-13: 978-0123875822.
503
504 Ayachit, U., 2015. *The ParaView Guide: A Parallel Visualization Application*, Kitware, ISBN
505 978-1930934306.
506

- Altamimi, Z., Rebischung, P., Métivier, L., Xavier, C., 2016. ITRF2014: A new release of the International Terrestrial Reference Frame modeling nonlinear station motions, *J. Geophys. Res. Solid Earth*, 121, doi:10.1002/2016JB013098.
- Argand, E., 1924. La tectonique de l'Asie. 104 p. Compte rendu du congrès géologique international (1922). Vaillant-Carmane press (Liege, Belgium).
- Avouac, J.P., Bollinger, L., Lavé, J., Cattin, R., Flouzat, M., 2001. Le cycle sismique en Himalaya, Comptes Rendus de l'Académie de Sciences - Serie Ila : Sciences de la Terre et des Planètes. doi:10.1016/S1251-8050(01)01573-7.
- Avouac, J.-P., Meng, L., Wei, S., Wang, T., Ampuero, J.P., 2015. Lower edge of locked Main Himalayan Thrust unzipped by the 2015 Gorkha earthquake. *Nature Geoscience*, ISSN 1752-0894.
- Baillard, C., Lyon-Caen, H., Bollinger, L., Rietbrock, A., Letort, J., Adhikari, L.B., 2017. Automatic analysis of the Gorkha earthquake aftershock sequence: evidences of structurally segmented seismicity. *Geophysical Journal International*, 209(2), 1111-1125.
- Barbot, S., Hamiel, Y., Fialko, Y., 2008. Space geodetic investigation of the coseismic and postseismic deformation due to the 2003 Mw 7.2 Altai earthquake: Implications for the local lithospheric rheology. *J. Geophys. Res.*, 113(B03403), doi:10.1029/2007JB005063.
- Barbot, S., Fialko, Y., Bock, Y., 2009. Postseismic deformation due to the Mw 6.0 2004 Parkfield earthquake: stress-driven creep on a fault with spatially variable rate-and-state friction parameters. *J. Geophys. Res.*, 114(B07405), doi:10.1029/2008JB005748.
- Barbot, S., Fialko Y., 2010. A unified continuum representation of postseismic relaxation mechanisms: semianalytic models of afterslip, poroelastic rebound and viscoelastic flow. *Geophys. J. Int.*, 182(3), 1124–1140, doi:10.1111/j.1365-246X.2010.04678.x.
- Barbot, S., Fialko, Y., 2010. Fourier-domain Green's function for an elastic semi-infinite solid under gravity, with applications to earthquake and volcano deformation. *Geophys. J. Int.*, 182(2), 568–582, doi:10.1111/j.1365- 246X.2010.04655.x.

541

542 Beaumont, C., Jamieson, R.A., Nguyen, M.H., Lee, B., 2001. Himalayan tectonics explained
543 by extrusion of a low-viscosity crustal channel coupled to focused surface denudation. *Nature*
544 414, 738–742.

545

546 Bettinelli, P., Avouac, J.-P., Flouzat, M., Bollinger, L., Ramillien, G., Rajaure, S., Sapkota, S.,
547 2008. Seasonal variations of seismicity and geodetic strain in the Himalaya induced by surface
548 hydrology. *Earth Planet. Sci. Lett.* 266, 332–344.

549

550 Berger, A., Jouanne, F., Hassani, R., Mugnier, J.L., 2004. Modelling the spatial distribution of
551 present-day deformation in Nepal: how cylindrical is the Main Himalayan Thrust in Nepal?
552 *Geophys. J. Int.*, 156, 94–114.

553

554 Bhattarai, M., Adhikari, L.B., Gautam, U.P., Laurendeau, A., Labonne, C., Hoste-Colomer, R.,
555 Hernandez, B., 2015. Overview of the large 25 April 2015 Gorkha, Nepal, earthquake from
556 accelerometric perspectives. *Seismological Research Letters*, 86(6), 1540-1548.

557

558 Bollinger, L., Sapkota, S.N., Tapponnier, P., Klinger, Y., Rizza, M., Van der Woerd, J., Tiwari,
559 D.R., Pandey, R., Bitri, A., Bes de Berc, S., 2014. Estimating the return times of great
560 Himalayan earthquakes in eastern Nepal: Evidence from the Patu and Bardibas strands of the
561 Main Frontal Thrust, *J. Geophys. Res. Solid Earth*, 119, doi:10.1002/2014JB010970.

562

563 Bollinger, L., Tapponnier, P., Sapkota, S.N., Klinger, Y., 2016. Slip deficit in central Nepal:
564 Omen for a repeat of the 1344AD earthquake ? *Earth, Planets and Space*, 68, 1-12, DOI
565 10.1186/s40623-016-0389-1.

566

567 Bruhat L., Barbot S., Avouac J.P., 2011. Evidence for postseismic deformation of the lower
568 crust following the 2004 Mw 6.0 Parkfield earthquake. *J. Geophys. Res. Solid Earth*, 116 (B8).

569

570 Dach, R., S. Lutz, P. Walser, P. Fridez (Eds); 2015: **Bernese GNSS Software Version**
571 **5.2**. User manual, Astronomical Institute, University of Bern, Bern Open Publishing.
572 DOI: 10.7892/boris.72297; ISBN: 978-3-906813-05-9.

573

Denolle, M.A., Fan, W., and Shearer, P.M., 2015. Dynamics of the 2015 M7.8 Nepal earthquake. *Geophys. Res. Lett.*, 42, 7467–7475, doi:10.1002/2015GL065336.

Devi E. Uma, Kumar P. and KumarM. Ravi, 2011, Imaging the Indian lithosphere beneath the Eastern Himalayan region, *Geophysical Journal International*, Volume 187, Issue 2, 1 November 2011, Pages 631–641, <https://doi.org/10.1111/j.1365-246X.2011.05185.x>

Dieterich, J.H., 1979. Modeling of rock friction: 1. Experimental results and constitutive equations. *J. Geophys. Res.*, 84, 2161-2168.

Duputel, Z., Vergne, J., Rivera, L., Wittlinger, G., Farra, V., Hetényi, G., 2016. The 2015 Gorkha earthquake: a large event illuminating the Main Himalayan Thrust fault. *Geophys. Res. Lett.* 43 (2517–2525), 2016G. <http://dx.doi.org/10.1002/L068083>.

Elliott, J., Jolivet, R., Gonzalez, P., Avouac, J.P., Hollingsworth, J., Searle, M.P., Stevens, V.L., 2016. Himalayan megathrust geometry and relation to topography revealed by the Gorkha earthquake. *Nature Geosci.* <http://dx.doi.org/10.1038/NGEO2623>.

Fan, W., Shearer, P.M., 2015. Detailed rupture imaging of the 25 April 2015 Nepal earthquake using teleseismic P waves. *Geophys. Res. Lett.* doi:10.1002/2015GL064587.

Fu, Y., Freymueller, J.T., 2012. Seasonal and long-term vertical deformation in the Nepal Himalaya constrained by GPS and GRACE measurements. *J. Geophys. Res.* 117, B03407. doi:10.1029/2011JB008925.

Grandin, R., Vallée, M., Satriano, C., Lacassin, R., Klinger, Y., Simoes, M., Bollinger, L., 2015. Rupture process of the Mw = 7.9 2015 Gorkha earthquake (Nepal): <http://dx.doi.org/10.1016/j.jseaes.2016.05.028> insights into Himalayan megathrust segmentation. *Geophys. Res. Lett.* 42 (20), 8373–8382.

Gualandi, A., Avouac, J.P., Galetzka, J., Genrich, J.F., Blewitt, G., Adhikari, L.B., Liu-Zeng, J., 2016. Pre-and postseismic deformation related to the 2015, Mw 7.8 Gorkha earthquake, Nepal. *Tectonophysics*, DOI: 10.1016/j.tecto.2016.06.014.

627

628 Hetényi, G., Vergne, J., Bollinger, L., & Cattin, R. (2011). Discontinuous low-velocity zones
629 in southern Tibet question the viability of the channel flow model. *Geological Society, London,*
630 *Special Publications*, 353(1), 99-108.

631

632 Hubbard, J., Almeida, R., Foster, A., Sapkota, S.N., Bürgi, P., Tapponnier, P., 2016. Structural
633 segmentation controlled the 2015 Mw 7.8 Gorkha earthquake rupture in Nepal. *Geology*, 44(8),
634 639-642.

635

636 Hugentobler U., Schaer S., Fridez, P., Bernese GPS Software Version 4.2. Astronomical
637 Institute, University of Berne, Switzerland, 2001.

638

639 Hutton, W., DeMets, C., Sánchez, O., Suárez, G., Stock, J., 2001. Slip dynamics during and
640 after the 9 October 1995 Mw = 8.0 Colima-Jalisco, Mexico. *Geophys. J. Int.*, 146, 637-658.
641 doi:10.1046/j.1365- 246X.2001.00472.x.

642

643 Jouanne, F., Mugnier, J.L., Gamond, J.F., Le Fort, P., Pandey, M., Bollinger, L., Flouzat, M.,
644 Avouac, J.P., 2004. Current shortening across the Himalayas of Nepal. *Geophys. J. Int.*, 157, 1-
645 14.

646

647 Jouanne, F., Awan, A., Madji, A., Pêcher, A., Latif, M., Kausar, A., Mugnier, J.L., Khan, I.,
648 Khan, N.A., 2011. Postseismic deformation in Pakistan after the 8 October 2005 earthquake:
649 evidence of afterslip along a flat north of the Balakot-Bagh Thrust. *J. Geophys. Res.*, **116**,
650 B07401, doi:[10.1029/2010JB007903](https://doi.org/10.1029/2010JB007903).

651

652 Jouanne F., Mugnier J.L., Sapkota S.N., Bascou B., Pecher A., 2017. Estimation of coupling
653 along the Main Himalayan Thrust in the central Himalaya. *Journal of Asian Earth Sciences*,
654 January 2017.

655

656 Kayal, J.R., 2008. Microearthquake Seismology and Seismotectonics of South Asia.
657 <http://dx.doi.org/10.1007/978-1-4020-8180-4>.

658

659 Kulhawy F.H, 1975. Stress deformation properties of rock and rock discontinuities,
660 *Engineering Geology*, Volume 9, Issue 4, pp. 327-350.

Kumar A., Singh S.K., Mitra S., Priestley K.F., Shankar Dayal, 2017. The 2015 April 25 Gorkha (Nepal) earthquake and its aftershocks: implications for lateral heterogeneity on the Main Himalayan Thrust. *Geophys. J. Int.*, 208 (2): 992-1008.

Lapusta, N., Rice, J., Ben-Zion, Y., & Zheng, G. (2000). Elastodynamic analysis for slow tectonic loading with spontaneous rupture episodes on faults with rate- and state-dependent friction. *Journal of Geophysical Research*, 105(B10), 23,765–23,789. <https://doi.org/10.1029/2000JB900250>.

Letort Jean, Laurent Bollinger, Helene Lyon-Caen, Aurélie Guilhem, Yoann Cano, Christian Baillard, Lok Bijaya Adhikari; Teleseismic depth estimation of the 2015 Gorkha–Nepal aftershocks, 2016, *Geophysical Journal International*, Volume 207, Issue 3, 1 December 2016, Pages 1584–1595, <https://doi.org/10.1093/gji/ggw364>.

Lindsey, E.O., Natsuaki, R., Xu, X., Shimada, M., Hashimoto, M., Melgar, D., Sandwell, D.T., 2015. Line-of-sight displacement from ALOS-2 interferometry: Mw 7.8 Gorkha Earthquake and Mw 7.3 aftershock. *Geophysical Research Letters* 42, 6655-6661. doi:10.1002/2015GL065385.

Melbourne, W.G., 1985. The case for ranging in GPS based geodetic systems. Paper Presented at 1st International Symposium on Precise Positioning with the Global Positioning System, Int. Assoc. of Geod., Rockville, Md.

Melnick, D., Moreno, M., Cisternas, M., Tassara, A., 2012. Darwin seismic gap closed by the 2010 Maule earthquake. *Andean Geology*, v. 39, no. 3, p. 558-563.

Mencin, D., Bendick, R., Upreti, B.N., Adhikari, D.P. Gajurel, A.P., Bhattarai, R.R., Shrestha, H.R., Bhattarai, T.N., Manandhar, N., Galetzka, J., Knappe, E., Pratt-Sitaula, B., Aoudia A., Bilham R., 2016. Himalayan strain reservoir inferred from limited afterslip following the Gorkha earthquake. *Nature Geoscience* , 9, 533-537. doi:10.1038/ngeo2734.

Moreno, M., Melnick, D., Rosenau, M., Baez, J., Klotz, J., Oncken, O., Tassara, A., Chen, J., Bataille, K., Bevis, M., Socquet, A., Bolte, J., Vigny, C., Brooks, B., Ryder, I., Grund, V. Smalley, B., Carrizo, D., Bartsch, M., Hase, H., 2012, Toward understanding tectonic control

on the Mw 8.8 2010 Maule Chile earthquake. *Earth and Planetary Science Letters*, v. 321-322, p. 152-165.

Mugnier, J.L., Huyghe, P., Gajurel, A., Upreti, B.N., Jouanne, F., 2011. Seismites in the Kathmandu valley and seismic hazard in central Himalaya. *Tectonophysics*. <http://dx.doi.org/10.1016/j.tecto.2011.05.012>.

Mugnier, J.L., Gajurel, A., Huyghe, P., Jouanne, F., Upreti, B.N., 2013. Structural interpretation of the great earthquakes of the last millennium in Central Himalaya. *Earth Sci. Rev.* 127, 30–47. <http://dx.doi.org/10.1016/j.earscirev.2013.09.003>.

Mugnier J.-L., Jouanne F., Bhattarai R., Cortes-Aranda J., Gajurel A., Leturmy P., Robert X., Upreti B., Vassallo R., 2017. Segmentation of the Himalayan megathrust around the Gorkha earthquake (25 April 2015) in Nepal. *Journal of Asian Earth Sciences*.

Nábělek, J., G. Hetényi, J. Vergne, S. Sapkota, B. Kafle, M. Jiang, H. Su, J. Chen, B. S. Huang, and the Hi-CLIMB Team (2009), Underplating in the Himalaya-Tibet collision zone revealed by the Hi-CLIMB experiment, *Science*, 325(5946), 1371–1374, doi:10.1126/science.1167719.

Nelson K. and 26 others, 1996. Partially molten middle crust beneath southern Tibet: synthesis of project INDEPTH results. *Science*, 274, 1684-1687.

Oldham, T., 1883. A catalogue of Indian earthquakes from the earliest time to the end of 1869 AD. *Mem. Geol. Survey India* 1, 163-215.

Ostini, L., Dach, R., Meindl, M., Schaer, S., Hugentobler, U., 2008. FODITS: a new tool of the Bernese GPS software. In: Torres, J.A., Hornik, H. (Eds.), *Proceedings of EUREF 2008 Symposium*, Brussels, Belgium.

Perfettini, H., Avouac, J.-P., 2004. Postseismic relaxation driven by brittle creep: A possible mechanism to reconcile geodetic measurements and the decay rate of aftershocks, application to the Chi-Chi earthquake, Taiwan. *J. Geophys. Res.*, 109, B02304, doi:10.1029/2003JB002488.

Rice, J. R., & Ben-Zion, Y. (1996). Slip complexity in earthquake fault models. *Proceedings of the National Academy of Sciences USA*, 93, 3811–3818.

Robert, X., Van Der Beek, P., Braun, J., Perry, C., Mugnier, J.L., 2011. Control of detachment geometry on lateral variations in exhumation rates in the Himalaya: insights from low-temperature thermochronology and numerical modeling. *J. Geophys. Res.: Solid Earth* 116, 1-22. doi:10.1029/2010JB007893.

Rousset, B., Barbot, S., Avouac J.P., Hsu, Y.J., 2012. Postseismic deformation following the 1999 Chi-Chi earthquake, Taiwan: Implication for lower-crust rheology, *J. Geophys. Res.: Solid Earth*, 117 (B12).

Ruina, A.L., 1983. Slip instability and state variable friction laws. *J. Geophys. Res.*, 88, 10,359-10,370.

Scholz, C.H., 1998. Earthquakes and friction laws. *Nature* 391, 37-42.

Szeliga, W., Hough, S., Martin, S., Bilham, R., 2010. Intensity, magnitude, location, and attenuation in India for felt earthquakes since 1762. *Bull. Seismol. Soc. Am.* 100, 570-584. <http://dx.doi.org/10.1785/0120080329>.

Wang, K., Fialko, Y., 2014. Space geodetic observations and models of postseismic deformation due to the 2005 M7.6 Kashmir (Pakistan) earthquake, *J. Geophys. Res.*, 119, 7306-7318.

Wang, K., & Fialko, Y. (2018). Observations and modeling of coseismic and postseismic deformation due to the 2015 *M_w* 7.8 Gorkha (Nepal) earthquake. *Journal of Geophysical Research:Solid Earth*, 123, 761–779. <https://doi.org/10.1002/2017JB014620>

Wessel, P., Smith, W.H.F., 1995. New version of the Generic Mapping Tools released, *EOS Trans. AGU*, 76, 329.

Wübbena, G., 1985. Software developments for geodetic positioning with GPS using TI4100 code and carrier measurements. Paper Presented at 1st International Symposium on Precise Positioning with the Global Positioning System, *Int. Assoc. of Geod.*, Rockville, Md.

Yu, S.-B., Hsu, Y.-J., Kuo, L.-C., Chen, H.-Y., Liu, C.-C., 2003. GPS measurement of postseismic deformation following the 1999 Chi-Chi, Taiwan, earthquake. *J. Geophys. Res.*, 108(B11), 2520, doi:10.1029/2003JB002396.

Zhao, W., Nelson, K.D., Che, J., Quo, J., Lu, D., Wu, C., Liu, X., 1993. Deep seismic reflection evidence for continental underthrusting beneath southern Tibet. *Nature*, 366, 555-559.

Zhao, B., Bürgmann, R., Wang, D., Tan, K., Du, R. & Zhang, R. (2017). Dominant Controls of Downdip Afterslip and Viscous Relaxation on the Postseismic Displacements Following the Mw7.9 Gorkha, Nepal, Earthquake. *Journal of Geophysical Research: Solid Earth*, 122(10), 8376-8401. doi:10.1002/2017JB014366.

Captions

Graphic abstract

Example of observed and simulated postseismic time series and test of mechanisms controlling the postseismic deformation, afterslip along the northern part of the upper flat, the ramp and the flower flat of the Main Himalayan Thrust (blue) or a combination of afterslip along the northern part of the upper flat and the ramp of the MHT and a viscous relaxation controlled by a low viscosity body centered on the lower flat of the MHT (red). The simulated time series are respectively drawn in blue and red.

Figure 1. Location of the Gorkha earthquake along the upper flat of the MHT. Dark purple for ramp geometry; pink, light purple, and green for fully locked, partial coupled, and ductile MHT, respectively; red for rupture zones. The rupture area is bounded by lateral ramps (Mugnier et al., 2017).

Figure 2. Description of inter and co-seismic deformation used for modeling the post-seismic deformation with Relax software. (a) Coupling along the Main Himalayan Thrust during the

interseismic period (before the Gorkha earthquake) (modified from Jouanne et al., 2017) and location of Gorkha earthquake indicated by yellow dash line (Grandin et al, 2015). CR indicates the location of the crustal ramp. (b) Coseismic slip distribution (adapted from Grandin et al., 2015) used as input for our numerical simulation.

Figure 3. Observed (Jouanne et al., 2017) and simulated interseismic velocities using the model proposed by Jouanne et al. (2017). Velocities are expressed in the India fixed reference frame.

Figure 4. Postseismic displacements following the Gorkha earthquake for the June 24, 2015–December 2016 period. The recorded displacements are corrected for interseismic displacements.

The rupture of the Gorkha earthquake is indicated by a blue line and the rupture of its main aftershocks, on May 12, 2016, is drawn with an orange line. The star indicates the nucleation of the Gorkha earthquake to the west of its rupture. The dashed green lines indicate the location of the Judi lineament (Kayal, 2008) that separates the main rupture zone from the nucleation area (Kumar et al., 2017) and, on the eastern side, the Gaurishankar lineament (Mugnier et al., 2017). Errors ellipses are drawn for a 95% confidence level. GNSS stations installed by our team for this study are indicated in blue and permanent GNSS stations of LDG are indicated in orange.

Figure 5. Southern components for the cGNSS station displacements, corrected from interseismic velocities and seasonal signals estimated during the period before the main shock or extrapolated for the new stations. The locations of cGNSS stations are indicated in Figure 2.

Figure 6. Eastern components for the cGNSS station displacements, corrected from interseismic velocities and seasonal signals estimated during the period before the main shock or extrapolated for the new stations. The locations of cGNSS stations are indicated in Figure 2.

Figure 7. Vertical components for the cGNSS station displacements, corrected from interseismic velocities and seasonal signals estimated during the period before the main shock or extrapolated for the new stations. We present only the time series that seem to be correctly correct for seasonal components. The locations of cGNSS stations are indicated in Figure 2.

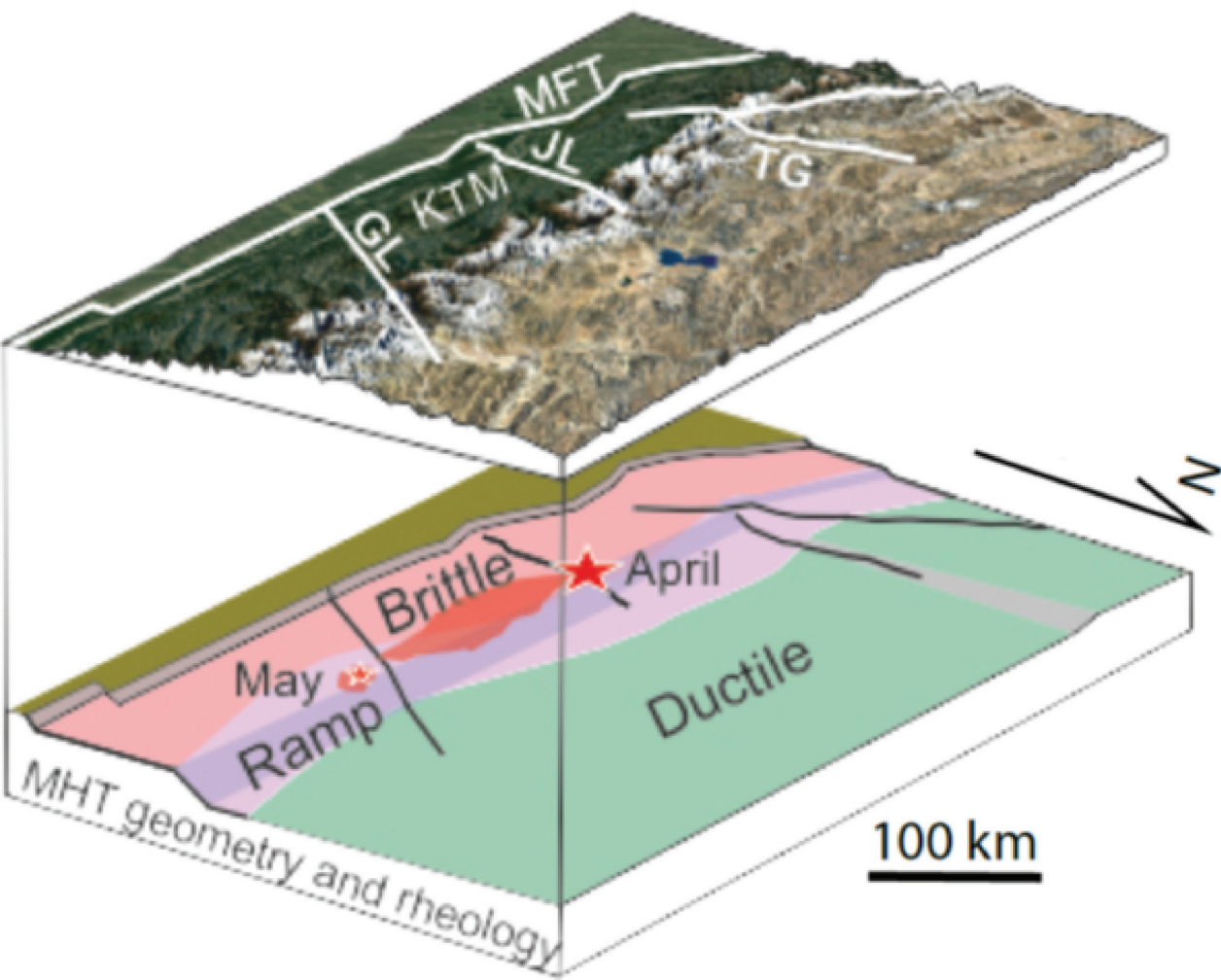
Figure 8. Geometry and rheological properties considered in the numerical simulations of postseismic deformation. (a) Viscous relaxation controlled by a high-fluidity body embedded in a half-space characterized by low fluidity; (b) afterslip along the northern part of the upper flat of the MHT, along the ramp, and along the lower flat of the MHT; and (c) viscous relaxation controlled by a high-fluidity body embedded in a half-space characterized by low fluidity and afterslip along the crustal ramp and along the northern part of the upper flat.

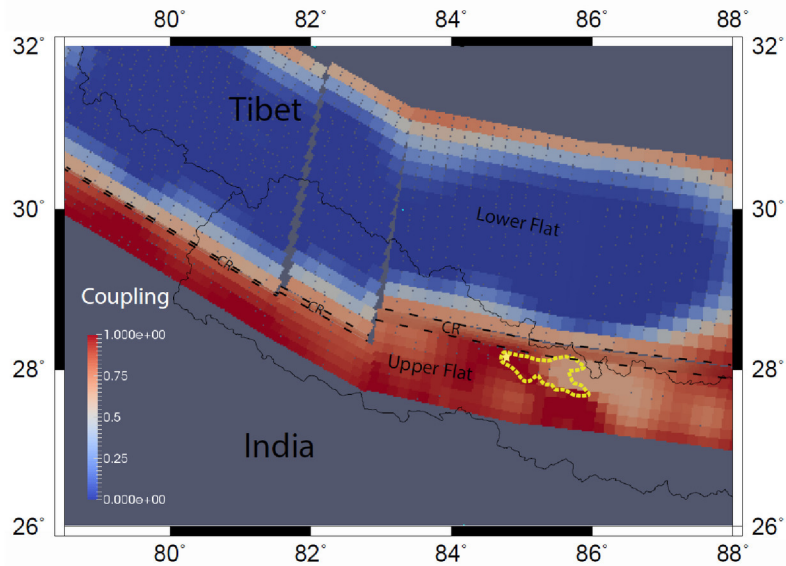
Figure 9. Search for the best solution, with the plot of the WRMS, for (a) the viscous relaxation hypothesis controlled by a viscous body along the lower flat of the MHT; (b) the afterslip hypothesis with (a-b) $\sigma = 10$ MPA; (c) the afterslip hypothesis with (a-b) $\sigma = 22$ MPA with the southern time series, (d) the afterslip hypothesis with (a-b) $\sigma = 22$ MPA with the vertical time series; (e) afterslip and viscous relaxation controlled by a viscous body along the lower flat of the MHT with the southern time series and (f) afterslip and viscous relaxation controlled by a viscous body along the lower flat of the MHT with the vertical time series .

Figure 10. Observed and simulated postseismic time series with our preferred afterslip model, the afterslip & viscous relaxation model, and the viscous relaxation model. The simulated time series with our preferred afterslip and afterslip & viscous relaxation models almost always become conflated. Blue curve: afterslip hypothesis, red curve: afterslip and viscous relaxation controlled by a viscous body along the lower flat of the MHT.

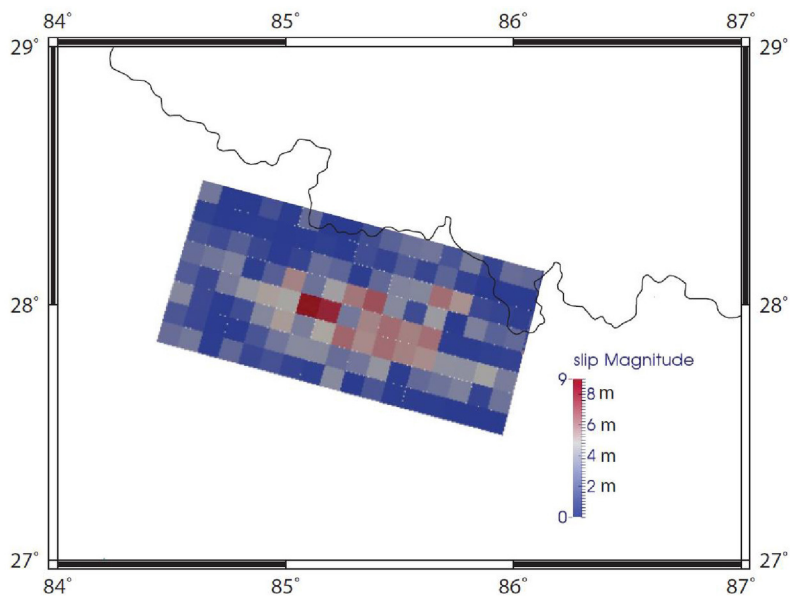
Figure 11. (a) Evolution of slip over time and space, predicted by our preferred afterslip model, expressed for selected dates. The locations of the permanent GNSS stations used to constrain our modeling are indicated by circles, (b) zoom of afterslip distribution after two years.

Fig. 12. Comparison between interseismic slip rate, seismic slip, and after-slip predicted after 6 years, supposed to be the end of postseismic deformation, along the Main Himalayan Thrust. See Fig. 9 for location of the cross section.

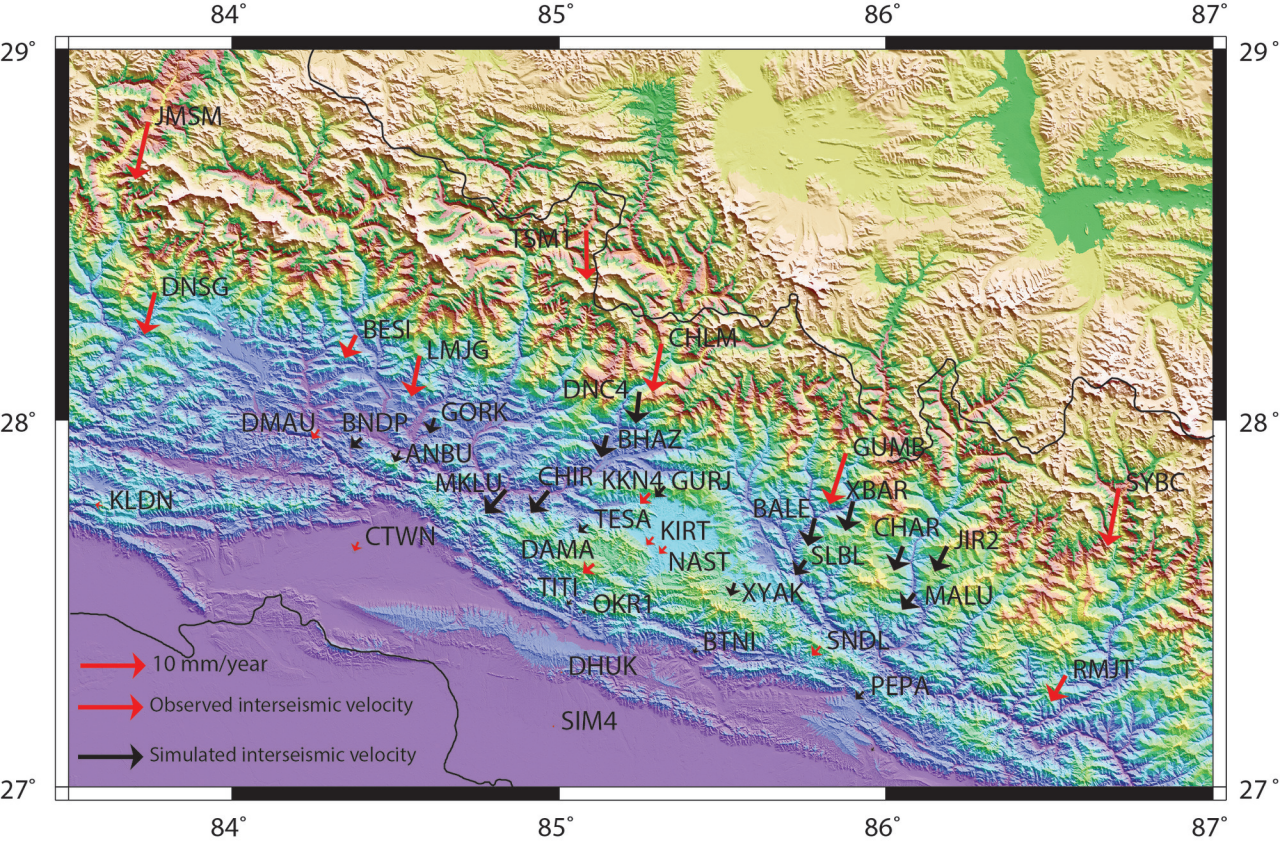


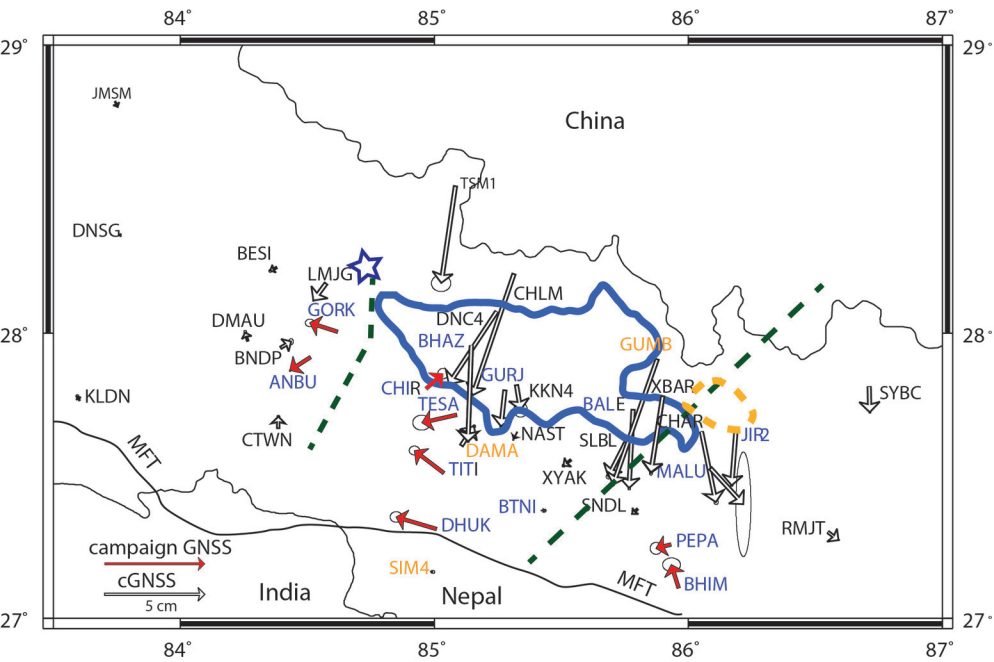


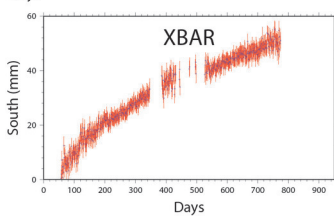
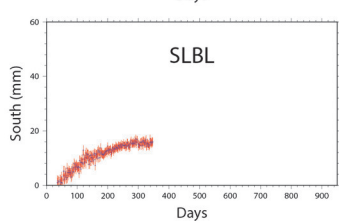
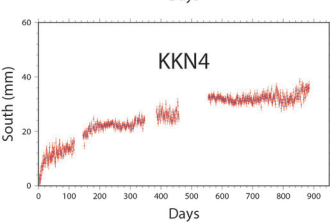
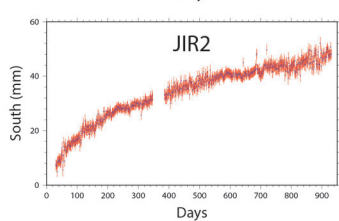
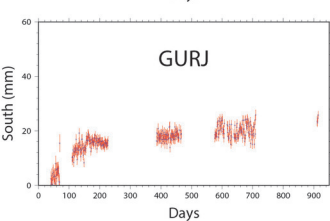
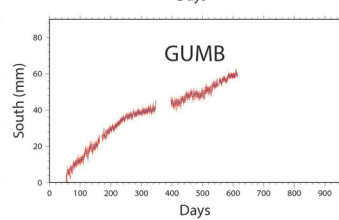
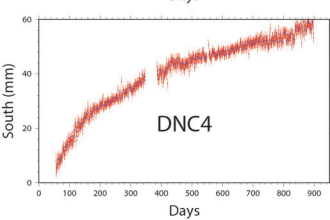
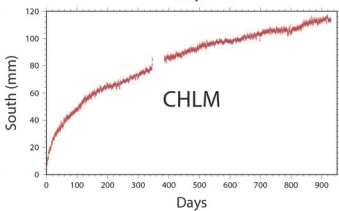
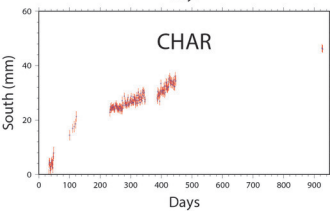
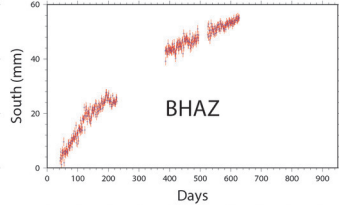
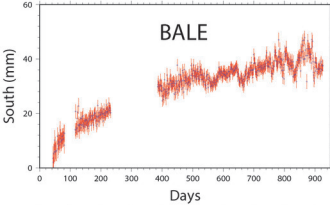
(a)

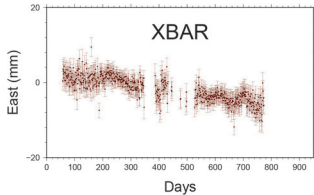
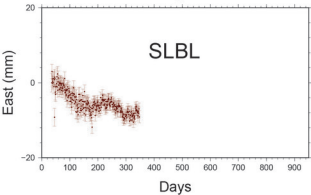
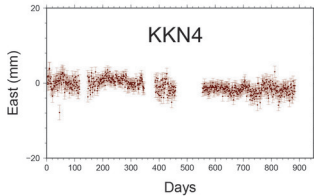
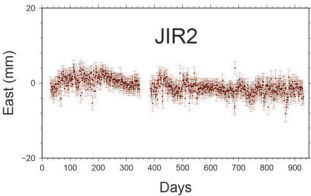
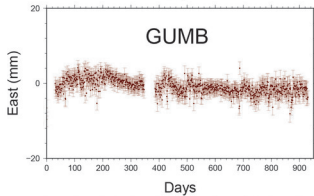
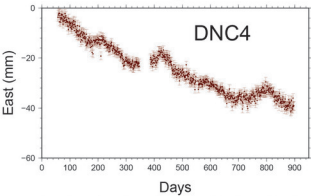
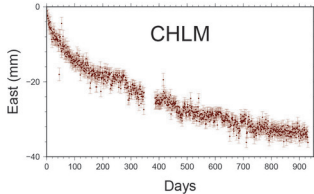
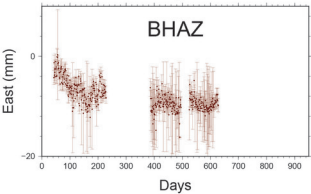
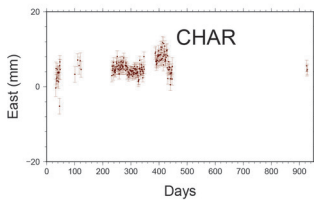
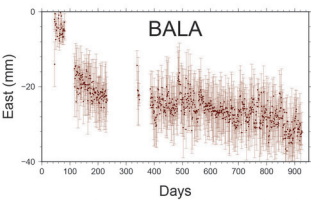


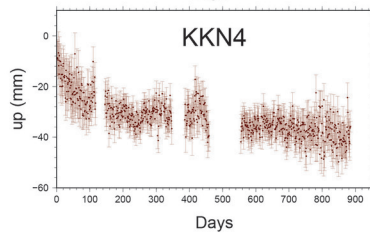
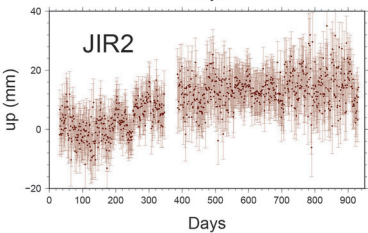
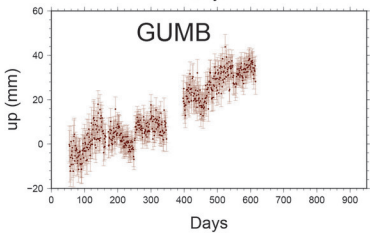
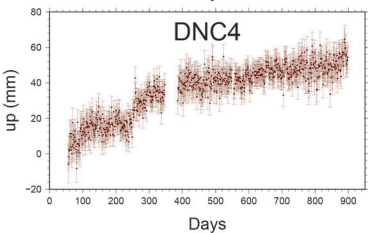
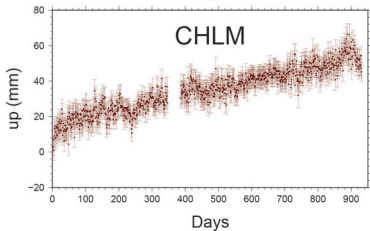
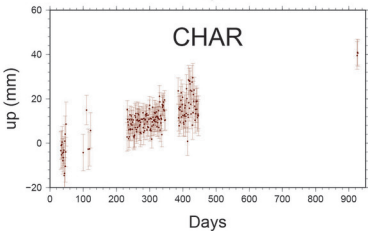
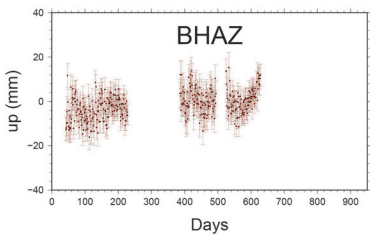
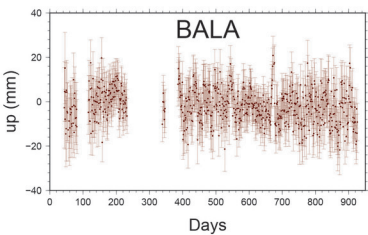
(b)

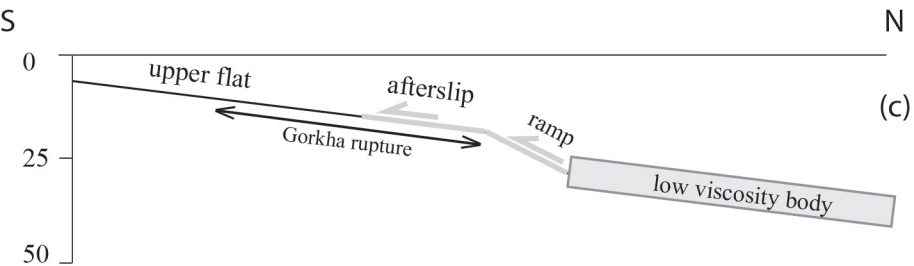
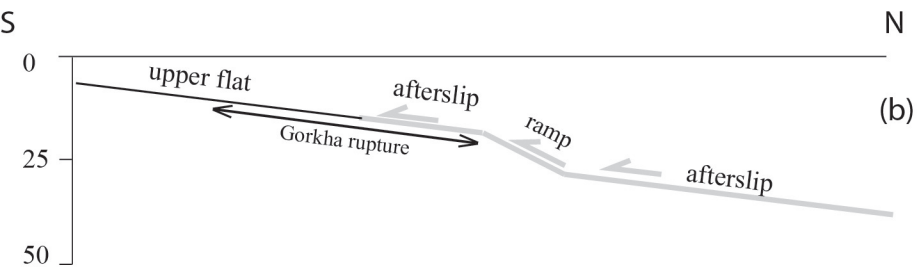
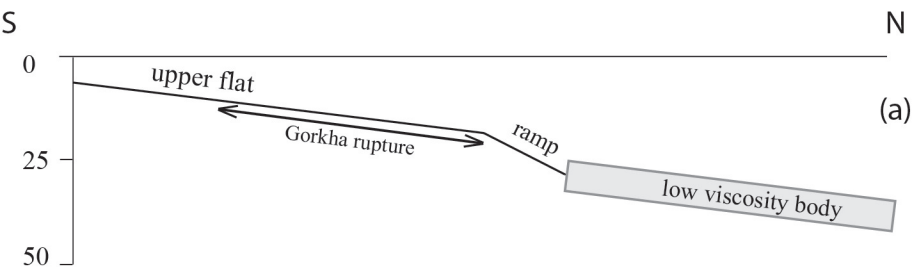




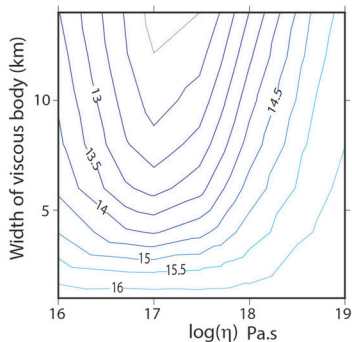




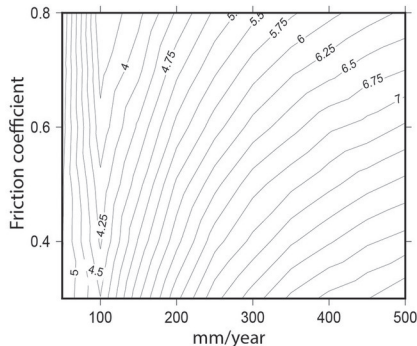




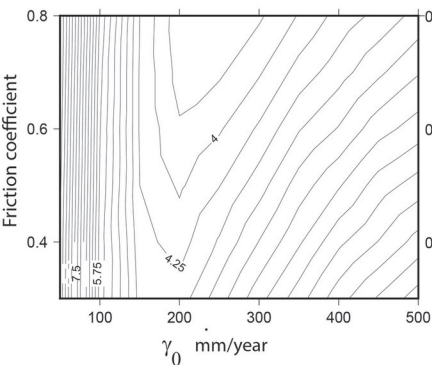
Viscous relaxation (a)



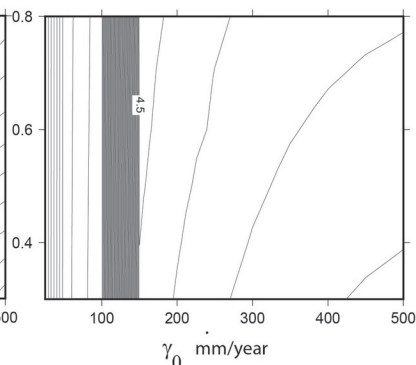
Afterslip 10 MPA (b)



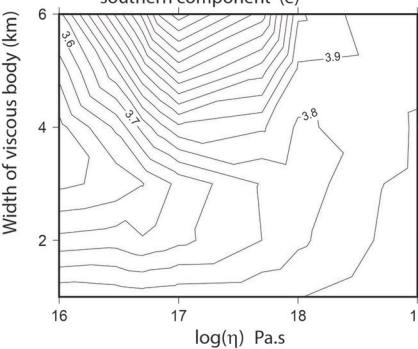
Afterslip 20 MPA southern component (c)



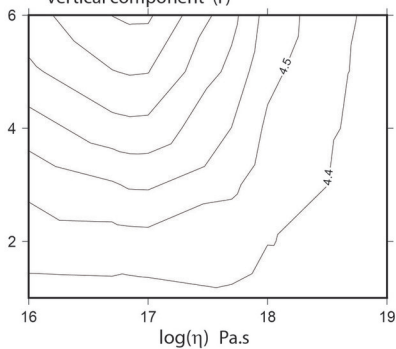
Afterslip 20 MPA vertical component (d)

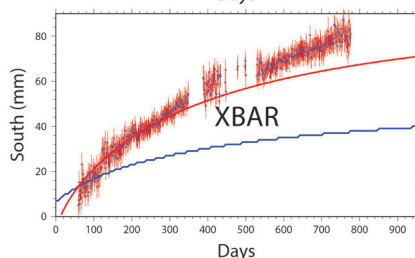
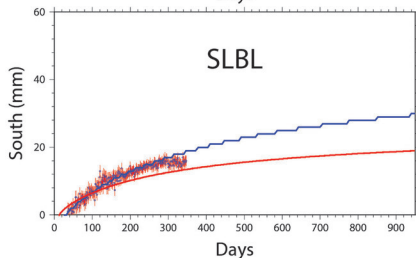
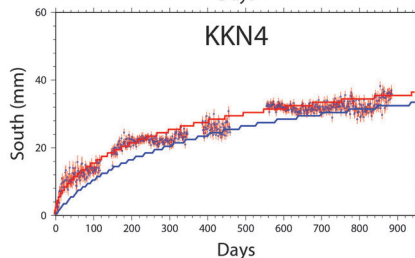
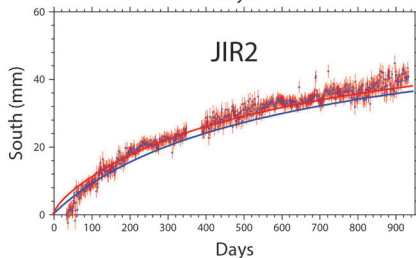
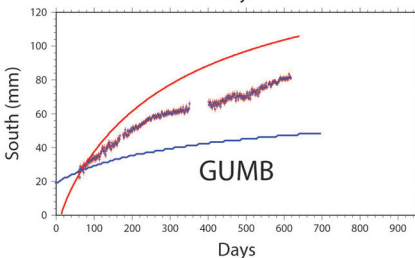
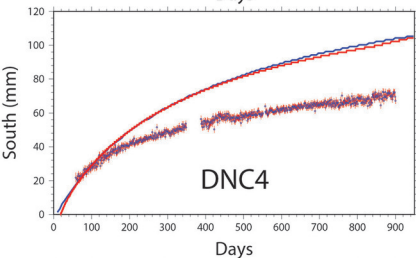
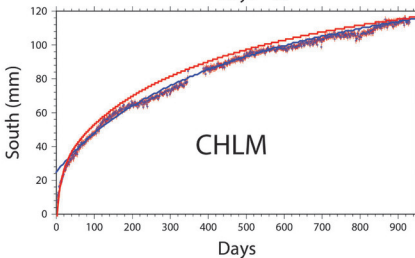
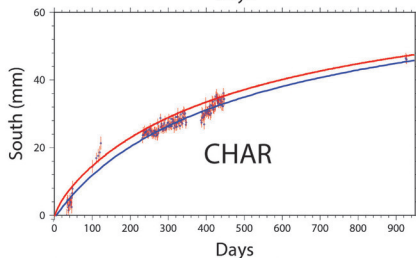
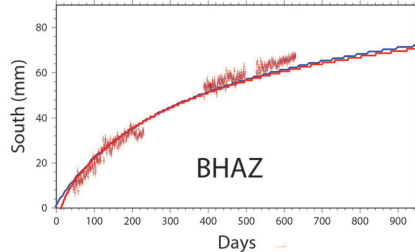
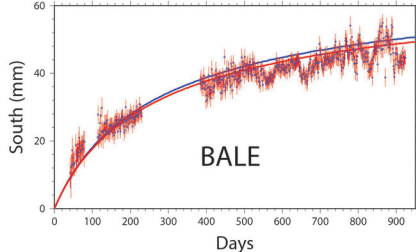


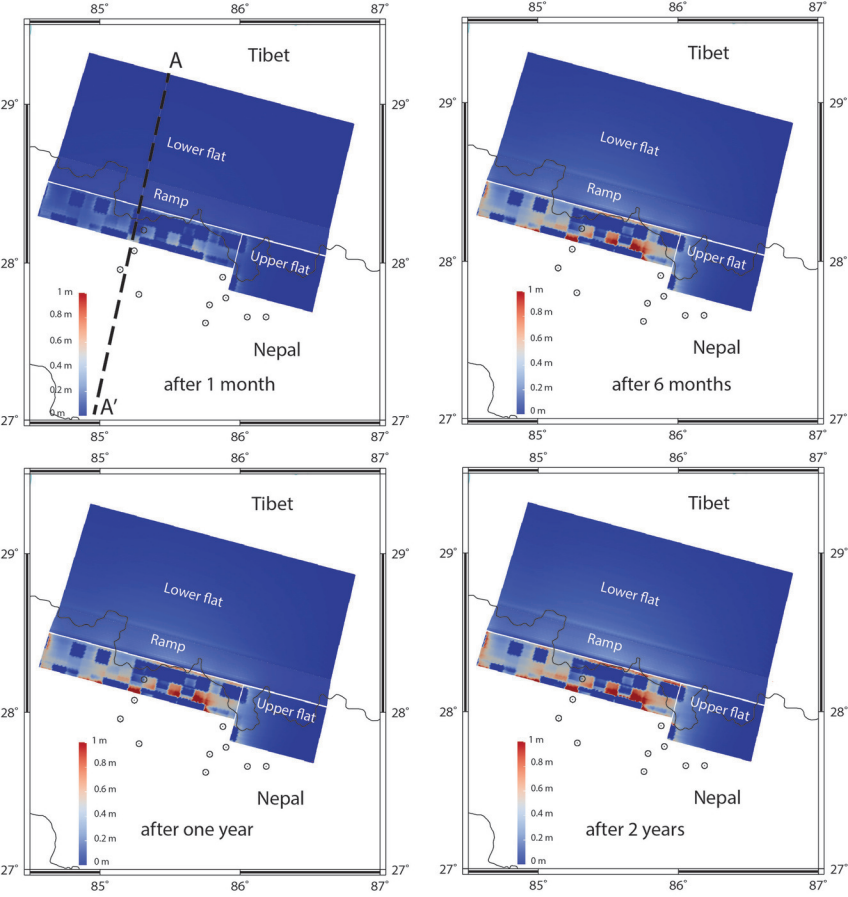
Afterslip and viscous relaxation southern component (e)



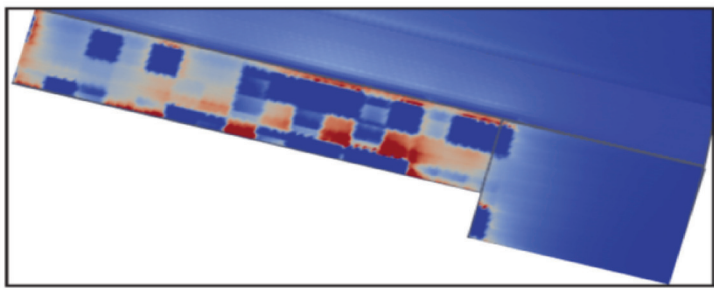
Afterslip and viscous relaxation vertical component (f)







(a)



(b)

